Quasi-solid-state electrolyte for rechargeable high-temperature molten salt iron-air battery

Shiyu Zhang, Yun Yang, Liwei Cheng, Jian Sun, Xiaomei Wang, Pengfei Nan, Chaomei Xie, Haisheng Yu, Yuanhua Xia, Binghui Ge, Jun Lin, Linjuan Zhang, Chengzhi Guan, Guoping Xiao, Cheng Peng, George Zheng Chen, Jian-Qiang Wang
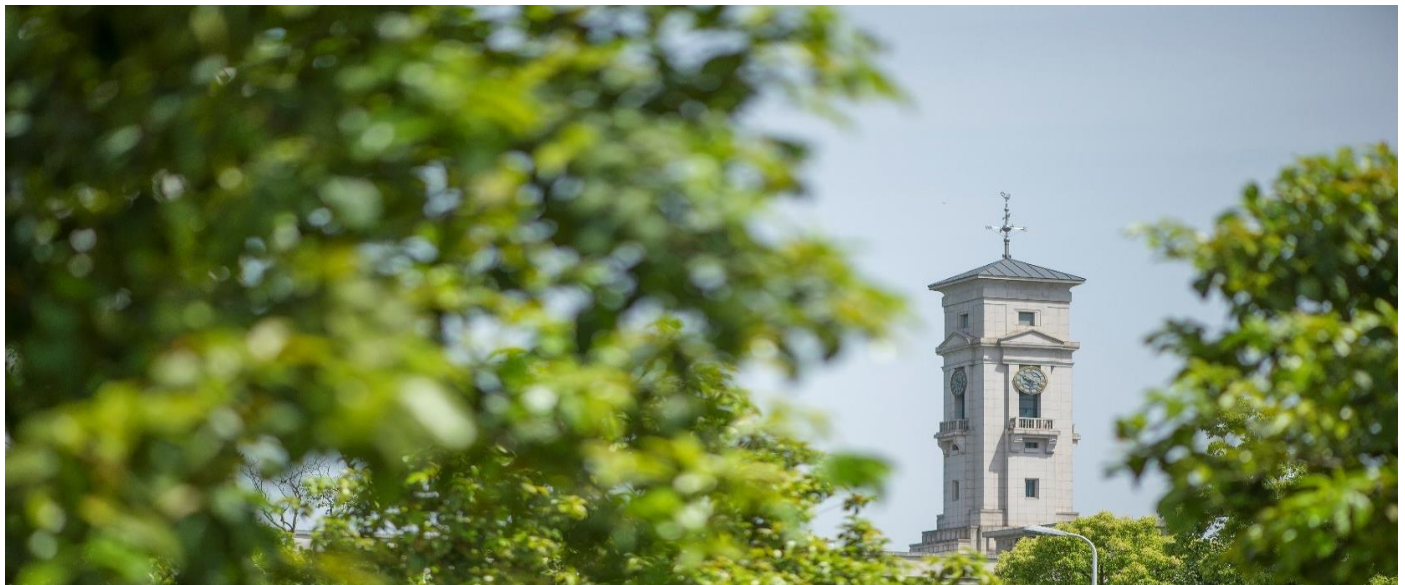
University of Nottingham
UK | CHINA | MALAYSIA

Quasi-solid-state electrolyte for rechargeable high-temperature molten salt iron-air battery

Shiyu Zhang[1,2]†, Yun Yang[1]†, Liwei Cheng[1,2]†, Jian Sun[1,2], Xiaomei Wang[1,2,4], Pengfei Nan[5], Chaomei Xie[6], Haisheng Yu[1], Yuanhua Xia[6], Binghui Ge[5], Jun Lin[1], Linjuan Zhang[1,3], Chengzhi Guan[1,3], Guoping Xiao[1,3], Cheng Peng[1, 2, 3]*, George Zheng Chen[7,8]*, Jian-Qiang Wang[1, 2, 3]*

[1]Key Laboratory of Interfacial Physics and Technology, Shanghai Institute of Applied Physics, Chinese Academy of Sciences, Shanghai 201800, China
[2]University of Chinese Academy of Sciences, No.19(A) Yuquan Road, Shijingshan District, Beijing 100049, China
[3]Dalian National Laboratory for Clean Energy, Dalian 116023, China
[4]State Key Laboratory of Radiation Medicine and Protection, School for Radiological and Interdisciplinary Sciences (RAD-X) and Collaborative Innovation Center of Radiation Medicine of Jiangsu Higher Education Institutions, Soochow University, Suzhou 215123, China
[5]Institute of Physical Science and Information Technology, Anhui University, Heifei, China
[6]Key Laboratory of Neutron Physics and Institute of Nuclear Physics and Chemistry, China Academy of Engineering Physics, 621999, Mianyang, China
[7]Department of Chemical and Environmental Engineering, Faculty of Engineering, University of Nottingham, University Park, Nottingham NG7 2RD, United Kingdom
[8]Department of Chemical and Environmental Engineering, Faculty of Science and Engineering, University of Nottingham Ningbo China, Ningbo 315100, China

†These authors contributed equally: Shiyu Zhang, Yun Yang, Liwei Cheng.

*E-mail: pengcheng@sinap.ac.cn, george.chen@nottingham.ac.uk, wangjianqiang@sinap.ac.cn.

Abstract

Molten salts are a unique type of electrolyte enabling high-temperature electrochemical energy storage (EES) with unmatched reversible electrode kinetics and high ion-conductivities, and hence impressive storage capacity and power capability. However, their high tendency to evaporate and flow at high temperatures challenges the design and fabrication of the respective EES devices in terms of manufacturing cost and cycling durability. On the other hand, most of these EES devices require lithium-containing molten salts as the electrolyte to enhance performances, which not only increases the cost but also demands a share of the already limited lithium resources. Here we report a novel quasi-solid-state (QSS) electrolyte, consisting of the molten eutectic mixture of Na_2CO_3-K_2CO_3 and nanoparticles of yttrium stabilized zirconia (YSZ) in a mass ratio of 1:1. The QSS electrolyte has relatively lower volatility in comparison with the pristine molten Na_2CO_3-K_2CO_3 eutectic, and therefore significantly suppresses the evaporation of molten salts, thanks to a strong interaction at the interface between molten salt and YSZ nanoparticles at high temperatures. The QSS electrolyte was used to construct an iron-air battery that performed excellently in charge-discharge cycling with high columbic and energy efficiencies. We also propose and confirm a redox mechanism at the three-phase interlines in the negative electrode. These findings can help establish a simpler and more efficient approach to designing low-cost and high-performance molten salt metal-air batteries with high stability and safety.

Keywords: molten salt iron-air battery, quasi-solid-state electrolyte, Na_2CO_3-K_2CO_3 eutectic, yttrium stabilized zirconia nanoparticles, three-phase interline.

Rechargeable molten salt batteries (MSBs) are a type of advanced high temperature electrochemical energy storage (EES) devices.[1-5] They are featured by ultra-high energy capacity and power capability, and outstanding durability and safety, and have the great potential for future large-scale utilization of clean and renewable energy to meet the growing global demand for sustainable energy supply.[6-9] Low-cost and inflammable inorganic molten salts are commonly utilized as the electrolytes in MSBs, for example, liquid metal batteries (LMBs) and molten air batteries (MABs).[10-17] The high working temperatures of molten salts are responsible for their extraordinarily high ion conductivity, and desirably fast kinetic and transport properties.[18-22] However, inorganic molten salts also possess adverse characteristics. At sufficiently high temperatures, molten salts can be aggressively corrosive[23,24] readily volatile and flowable,[25] which are disadvantageous to battery design as well as safety and stability. It is an urgent demand on electrolyte design, tuning these characteristics for better battery performance.

Quasi-solidification is an effective strategy of electrolyte design to overcome the disadvantages of electrolyte leakage and volatilization in room-temperature batteries with liquid electrolytes. The well-designed quasi-solid-state (QSS) electrolyte performs high ionic conductivity and electrochemical stability, low combustibility as well as high mechanical strength, thus have been extensively exploited in advanced lithium-based and sodium-based batteries.[26-31] Among these QSS electrolytes, ceramic nanopowders have been successfully utilized as the auxiliary filler for the enhancement of mechanical strength and ion conductivity.[31,32] Herein, we present a new class of high-temperature QSS molten salt electrolyte based on nanosized solid oxide fillers as a new MSB-customized multifunctional electrolyte beyond conventional molten salt electrolytes. As a proof-of-concept of the high-temperature QSS electrolyte, its potential application to rechargeable high-temperature molten salt iron-oxygen batteries (MIBs) is explored with particular attention to the volatility and flowability of molten electrolyte. So far, to the best of our knowledge, this is the first report on QSS molten electrolyte for high-temperature MSBs.

As representative molten electrolytes, alkali carbonates and their eutectics have been used in MIBs because they can deliver not only high oxide ion conductivities in a wide temperature range, but also favorable electrochemical potential windows to match iron redox reactions.[11,12,14,17] However, these molten carbonates are volatile at high temperatures, causing electrolyte loss, whilst their easy flowability increases the risk of leakage and also restricts the operation flexibility of the battery. In order to reduce their volatility and flowability, molten salts can be mixed with the powder of an appropriate oxide. It was thought that at sufficiently high contents (e.g. beyond the peculation content), the powder particles could form a flexibly connected network to physically restrict convection (flow) and evaporation of the molten salts. This approach might however sacrifice some ionic conductivity of the molten salts, but such a loss can be compensated by using the powder of a solid ion conductor. In this work, nanoparticles of the solid oxide ion conductor, yttrium stabilized zirconia (YSZ), were mixed with the eutectic mixture of Na_2CO_3 and K_2CO_3 (NaK, with the calculated viscosity value of 5.09×10^{-4} cP, Fig. S1). It was found that at a mass ratio of 1:1, the YSZ-NaK mixture reached a paste-like quasi-solid state when the applied temperature was above the melting temperature of the eutectic (ca. 703 □). This phenomenon is considered to have resulted from the YSZ nanoparticles interacting strongly at their interfaces with

the molten carbonate salts, further suppressing the volatility and flowability of the latter.

This novel QSS electrolyte facilitated the design and construction of a simple and effective high temperature rechargeable iron-air battery that was tested successfully in terms of key performance parameters, namely storage capacity, power capability, cyclic charge-discharge stability and energy efficiency, and materials and manufacturing affordability. In addition, redox reactions responsible for charging and discharging the negative electrode were revealed to proceed at, and via the propagation of the metal-oxide-molten salt three phase interlines (3PI). These findings should form the basis for the establishment of a generic design of molten salt electrolytes to restrain their flow and volatile characteristics in high-temperature EES device.

In this work, firstly, we designed and constructed a laboratory MIB with an YSZ supported silver positive electrode, a hematite (Fe_2O_3) coated silver negative electrode, and the QSS electrolyte consisting of the molten NaK eutectic and YSZ nanoparticles, as schematically depicted in Fig. 1. The YSZ nanoparticles had a diameter ranging from 40 to 400 nm (Fig. S2). Fig. S3 shows the wetting angle between YSZ sheet and molten NaK is ~30°. At a mass ratio 1:1, the NaK-YSZ mixture was nonflowing but could be extruded to certain shapes at temperatures above the melting point of the NaK eutectic (Fig. S4). The photographs of NaK-YSZ mixtures with different mass ratios at 800 □ (vertical view) and room temperature (vertical and side view) are shown in Fig. S5. The electrochemical impedance spectra (EIS) in Fig. S6 demonstrate that the conductivity of QSS electrolyte was ~0.22 S/cm, a little lower than that of molten NaK electrolyte (~0.42 S/cm).

Fig. 2 presents the microstructure of the solidified QSS electrolyte characterized by transmission electron microscopy (TEM) and energy dispersive spectrometer (EDS) mapping analysis after a high-temperature treatment at 800 □. The TEM image of smashed QSS electrolyte in Fig. 2b reveals the formation of a core-shell structure between molten NaK and YSZ nanoparticles, with the measured average shell thickness of less than 10 nm. The magnified TEM image with the EDS analysis of an overlay of the obtained elemental mapping in Fig. 2e-h confirms the composition of the core-shell structure and also shows YSZ nanoparticles being encapsulated by the NaK eutectic. Moreover, further magnified high-resolution TEM images present clearly the interface between a highly crystalline YSZ nanoparticle and the layer of amorphous binary eutectic NaK, indicating the strong interaction between YSZ nanoparticles and the NaK eutectic (Fig. 2b-d).

To investigate the volatility of the QSS electrolyte, thermogravimetry (TG) analysis was applied with a dynamic heating mode and a successive constant temperature mode. As shown in Fig. 3a, YSZ nanoparticles were thermally stable at 800 □, whereas visible weight losses occurred on the TG curves of both the NaK eutectic and QSS electrolyte when the temperature was raised beyond the NaK eutectic melting point of 703 □. It implies that evaporation of molten NaK was the essential cause for the weight loss at high temperatures. Furthermore, the weight losses of the QSS electrolyte and NaK eutectic at the stage of the constant temperature mode were 4.29 % (with a weight loss rate of 1.29 mg min^{-1}) and 6.51% (with a weight loss rate of 1.97 mg min^{-1}), respectively. Both the less weight loss and the lower weight loss rate indicate that the volatilization of QSS electrolyte was less than that of the NaK eutectic at high temperatures.

Further, the vapor pressures of both the QSS electrolyte and molten NaK were measured to evaluate the energy of evaporation. Because both the QSS electrolyte and molten NaK should start to evaporate at and above 703 □, the vapor pressure measurement was carried out from an initial steady state at 700 □ to another steady state at higher temperatures in a pre-evacuated sealable tubular furnace with a relatively low pressure to diminish the influence (e.g. thermal expansion) of residual air. Fig. 3c shows the measured vapor pressures at different temperatures. As the temperature rose from 700 □ to 1100 □, the vapor pressure of the QSS electrolyte increased from 3 kPa to 64 kPa, whereas that of the NaK eutectic from 2 kPa to 132 kPa. This difference is direct evidence that the QSS electrolyte is less volatile than the NaK eutectic. Assuming the molten salt vapor as an ideal gas, the energy of evaporation was derived according to the Clausius-Clapeyron equation without consideration of the residual air in the sealed furnace. The energy of evaporation for the QSS electrolyte was 92 kJ mol^{-1}, higher than that of 74 kJ mol^{-1} for the NaK eutectic (Fig. S7). As discussed above, the higher value of energy of evaporation of the QSS electrolyte may be attributed to the YSZ nanoparticles not only forming a flexible network to physically retard evaporation, but also interacting strongly with, and hence withholding the salt ions, particularly the oxygen containing anions (e.g. O^{2-} and CO_3^{2-}) from escaping as a vapor.

In order to study the interaction between YSZ nanopowders and molten NaK, we carried out high-temperature in situ studies on the QSS electrolyte. High-resolution neutron powder diffraction (HRND) spectra revealed the bulk-phase structure of the QSS electrolyte at 800 □ (Fig. S8). In comparison with the HRND spectra at room temperature, the vanished diffraction peaks of the NaK eutectic indicates the phase transition of the NaK eutectic from crystalline solid to liquid at 800 □. Furthermore, the well-retained diffraction peaks at 36.8°, 74.2°, 104.8° and 125.9° of tetragonal zirconia (*t*-ZrO$_2$) indicate the state of YSZ nanoparticles in the QSS electrolyte at 800 □. These findings agree with the QSS electrolyte being a solid-liquid mixture of YSZ nanoparticles and molten NaK at 800 □.

High-resolution Raman spectra further revealed the refined structure at the interface between YSZ nanoparticles and the liquid NaK eutectic in the QSS electrolyte at 800 □ (Fig. 3b). In detail, the characteristic peaks at 142 cm^{-1}, 324 cm^{-1}, and 594 cm^{-1} on the Raman spectrum of the QSS electrolyte correspond to *t*-ZrO$_2$, and those at 169 cm^{-1}, 180 cm^{-1}, and 367 cm^{-1} belong to monoclinic zirconia (*m*-ZrO$_2$).[33,34] In comparison, the Raman spectrum of pristine YSZ nanoparticles only showed the characteristic peaks of *t*-ZrO$_2$, without any sign for *m*-ZrO$_2$. It clearly indicates that part of *t*-ZrO$_2$ had transformed to *m*-ZrO$_2$, and this could have happened at the interface between YSZ nanoparticles and molten NaK. Such a phase transformation might be attributed to the loss of yttrium in zirconia lattice driven by the concentration gradient between YSZ nanoparticle and molten NaK. It is likely that yttria on the surface of YSZ nanoparticles became less stable and tends to diffuse into molten NaK. Consequently the YSZ phase transformed from tetragonal to monoclinic upon losing yttria. Moreover, more remarkable characteristic peaks of *m*-ZrO$_2$ were shown by the Raman spectrum of the solidified QSS electrolyte at room temperature (Fig. S9). The room-temperature X-ray diffraction (XRD) pattern of the solidified QSS electrolyte (Fig. 3d) further confirmed the formation of *m*-ZrO$_2$, showing diffraction peaks at 28.17° and 31.46° that correspond to the crystal planes of (-111) and (111) of *m*-ZrO$_2$, respectively (JCPDS 37-1484). Additionally, the characteristic peaks of *t*-ZrO$_2$ were

significantly stronger than those of m-ZrO$_2$, indicating the phase of t-ZrO$_2$ was still dominant in the solidified QSS electrolyte.

A laboratory QSS-MIB was constructed in a vertical tubular furnace at 800 °C and studied for its cyclic charging-discharging behavior in the constant current mode (Fig. S10). The charging current density was 4 mA cm^{-2}, but the discharging current density varied between 2, 1.5, 1 and 0.5 mA cm^{-2} with a cutoff cell voltage of 0.3 V. The columbic efficiency (CE) remained above 90% (Fig. 4a) and the energy efficiency (EE) of the QSS-MIB increases from 52.1% to 61.2% (Fig. 4b) when the discharging current decreased from 2 to 0.5 mA cm^{-2}. Fig. 4c further shows that CE remained above 90% when the utilization of hematite increased from 11.8% to 75%. As shown in Fig. S11, the EE value of QSS-MIB was 37.56% when the utilization of hematite reached 75%, thus we calculated that the output energy density of QSS-MIB was 380.3 Wh Kg^{-1}. Fig. 4e shows that the cell voltage profile gradually decreased as the discharging current density increased from 0.5 mA cm^{-2} to 2 mA cm^{-2}, yet the specific capacity remained at ~1300 mAh g^{-1} based on the mass of iron on the negative electrode, close to the theoretical specific capacity of 1430 mAh g^{-1}. Cycling charge/discharge results in Fig. 4f illustrates that both the CE and EE values of the QSS-MIB increased rapidly before the 10th charge/discharge cycle, and then in the following cycles remained steady above 90% and 50%, respectively, with the hematite utilization of 11.8%. Moreover, Fig. 4d shows that all the charge/discharge curves from the 20th to the 80th cycles are identical with approximately the same discharge specific capacity of ca. 1300 mAh g^{-1}, suggesting a high stability of the QSS-MIB. After the 80th charge/discharge cycle, the continuous operation time of QSS-MIB reached 113 h whereas the weight loss of the whole battery with an initial weight of 200.28 g was merely 1.69 g. In comparison with the bi-phase electrolyte structured MIB in our previous work, most of the key performance parameters of QSS-MIB have been significantly improved, including a two orders of magnitude higher cycling stability and hematite utilization, and almost one time higher energy efficiency, as shown in Table S1.

Fig. 5a shows the scanning electron microscopy (SEM) image of the solidified QSS electrolyte on the negative electrode after cycling charge/discharge. A distinctive 10 μm layer on the surface of the QSS electrolyte. Energy-dispersive X-ray (EDX) results further demonstrated the distribution of Fe, Zr, Na and K near the interface between the QSS electrolyte and the distinctive layer (Fig. S12). It showed that Fe was highly accumulated near the negative electrode, and well-confined in the distinctive layer, instead of dispersing in the whole QSS electrolyte. This was probably because of the low solubility of iron oxides in the NaK eutectic. Furthermore, the distinctive layer also contained high levels of Na and K, indicating that Fe-oxides on the surface of silver electrode would be surrounded by molten NaK at 800 □ and consequently the liquid-solid-solid 3PI would have formed between molten NaK, iron oxides and silver electrode during QSS-MIB operation.

Cyclic voltammograms (CVs) were recorded to compare the behavior of the negative electrode in the QSS electrolyte at 800 □, and a pristine silver electrode but was not loaded iron oxide. The results are presented in Fig. 5b. The CV of the negative electrode showed a pair of current peaks in the range from ~0.35 to ~1.30 V, corresponding to the redox conversion between Fe (0) and Fe (III) in the iron oxide electrode. Moreover, the asymmetric CV of the negative electrode differed from that of the iron-oxygen battery with molten lithium carbonate (Li$_2$CO$_3$) in which the electrochemical deposition-dissolution mechanism of iron was responsible charging-discharging

of the negative electrode. Thus, a different redox conversion mechanism should have taken place in the QSS-MIB. Based on SEM and EDX analyses, the features on the CV of the negative electrode may be attributed to solid state redox conversion between Fe (0) and Fe (III) proceeded via a liquid-solid-solid 3PI mechanism on the negative electrode (Fig. S13).

To determine the active reduction and oxidation products in the QSS-MIB, the composition of the QSS electrolyte on the negative electrode was investigated after charging and discharging, respectively. As it can be seen in Fig. S14, the XRD pattern after charging the battery presents a peak at 44.75° which agrees that for the (1 1 0) crystal plane in the cubic Fe (0) phase (JCPDS 06-0696). In fact, the detection of Fe (0) was expected from reduction (charging) of Fe_2O_3 on the negative electrode. However, the characteristic diffraction peak of Fe metal vanished in the XRD spectrum after discharging the battery. The diffraction peaks at 28.44°, 31.56° and 38.21° correspond to the crystal planes of (1 0 6), (1 0 7), and (2 0 4) in the hexagonal phase of $K_2Fe_{22}O_{34}$, and those at 20.77°, 26.11° and 29.38° should belong to the crystal planes of (0 1 1), (1 1 1) and (1 2 0) in the orthorhombic phase of $NaFeO_2$, according JCPDS cards 31-1034 and 13-0521, respectively. It suggests that $K_2Fe_{22}O_{34}$ and $NaFeO_2$ are the oxidation (discharging) products on the negative electrode of the QSS-MIB.

Fig. 5c shows the Mössbauer spectra of the solidified QSS on the surface of the negative electrode at room temperature. Specific values of the isomeric shift (IS), quadrupole splitting (QS), and magnetic hyperfine field (HF) are displayed in Table S2. According to the fitting results, the Mössbauer spectrum of the composition on the charged negative electrode revealed three magnetic phases and a quadrupole doublet phase.[35,36] The magnetic phase with the IS value of zero and MF value of 32.78 corresponds to Fe (0), as the reduction (charging) product. The other couple of magnetic phases correspond to the spinel-type of potassium ferric ($K_2Fe_{22}O_{34}$), whilst the quadrupole doublet phase with the IS value of 0.35 and QS value of 0.53 can be related to sodium ferrate ($NaFeO_2$), both of them are the expected oxidation (discharging) products. After discharging, the magnetic phase of Fe (0) disappeared, accompanied by the increasing appearance of the magnetic phases of spinel-type potassium ferrite, suggesting the Fe (0) phase was oxidized to $K_2Fe_{22}O_{34}$ and $NaFeO_2$. The Fe K-edge X-ray absorption fine structure (XAFS) results firmly verified the redox conversion between Fe (0) and Fe (III) in $K_2Fe_{22}O_{34}$ and $NaFeO_2$ (Fig. 5d).[37,38] The obvious pre-edge peak in the normalized X-ray absorption near-edge structure (XANES) spectrum of the charged sample strongly suggests the existence of metallic Fe, and correspondingly, the Fourier transform of EXAFS (Fig. 5e) of the charged sample gave the Fe-Fe bond distance of ~2.17 nm that is similar to that of the Fe-Fe bond in iron foil. By contrast, the normalized XANES spectrum of the discharged sample presents a far higher proportion of Fe (III) state, suggesting the oxidation conversion from Fe (0) to Fe (III) when discharging the QSS-MIB. The reaction mechanism of QSS-MIB can be summarized as following:

Positive electrode: $3/4 O_2 + 3e^- \leftrightarrow 3/2 O_2^-$

Negative electrode: $Fe + 2 O^{2-} \leftrightarrow FeO_2^- + 3e^-$

In closing, we note that one long-standing challenge of molten salt metal air battery is to avert the volatility and fluidity of high-temperature molten salt electrolytes for improving their safety and stability. The QSS electrolyte constructed from molten salts and solid oxide nanopowders offers

the possibility to suppress the evaporation and flow of molten salts, via a strong interaction at the interface between solid oxide nanopowders and molten salts. The QSS-MIB we have presented here offers excellent cycling charge-discharge abilities with high columbic and energy efficiencies in non-lithium molten salts, and a liquid-solid-solid 3PI related electrochemical redox reaction that differs from the reversible deposition-dissolution mechanism in lithium-contained molten salts. Our encouraging results may boost further development of low-cost and high-performance molten salt metal air batteries with promising stability and safety by further and smart engineering of the quasi-solid-oxide electrolyte materials.

References

[1]   H. Kim, D.A. Boysen, J.M. Newhouse, B.L. Spatocco, B. Chung, P.J. Burke, D.J. Bradwell, K. Jiang, A.A. Tomaszowska,K. Wang, Liquid Metal Batteries: Past, Present, and Future, Chem. Rev. 113(2013) 2075-2099. doi:10.1021/cr300205k.

[2]   Z.G. Yang, J.L. Zhang, M.C.W. Kintner-Meyer, X.C. Lu, D.W. Choi, J.P. Lemmon,J. Liu, Electrochemical Energy Storage for Green Grid, Chem. Rev. 111(2011) 3577-3613. doi:10.1021/cr100290v.

[3]   G.S. Li, X.C. Lu, J.Y. Kim, K.D. Meinhardt, H.J. Chang, N.L. Canfield,V.L. Sprenkle, Advanced intermediate temperature sodium-nickel chloride batteries with ultra-high energy density, Nat. Commun. 7(2016) 10683. doi:10.1038/ncomms10683.

[4]   X.C. Lu, B.W. Kirby, W. Xu, G.S. Li, J.Y. Kim, J.P. Lemmon, V.L. Sprenkle,Z.G. Yang, Advanced intermediate-temperature Na-S battery, Energy Environ. Sci. 6(2013) 299-306. doi:10.1039/c2ee23606k.

[5]   G.Z. Chen, Supercapattery: Merit merge of capacitive and Nernstian charge storage mechanisms, Curr. Opin. Electroche. 21(2020) 358-367. doi:10.1016/j.coelec.2020.04.002.

[6]   B. Cui, Y. Shao, W. Xiang, S. Liu, X. Liu, W. Han, J. Zhang,S. Licht, A Nano PdO Activated Iron Molten Air Battery, J. Phy. Chem. C 122(2018) 8109-8115. doi:10.1039/c4ta01290a.

[7]   S. Licht, B. Cui, J. Stuart, B. Wang,J. Lau, Molten air- a new, highest energy class of rechargeable batteries, Energy Environ. Sci. 6(2013) 3646-3657. doi:10.1039/c3ee42654h.

[8]   K.L. Wang, K. Jiang, B. Chung, T. Ouchi, P.J. Burke, D.A. Boysen, D.J. Bradwell, H. Kim, U. Muecke,D.R. Sadoway, Lithium-antimony-lead liquid metal battery for grid-level energy storage, Nature 514(2014) 348-351. doi:10.1038/nature13700.

[9]   R.J. Bones, J. Coetzer, R.C. Galloway,D.A. Teagle, A Sodium Iron(II) Chloride Cell With A Beta-Alumina Electrolyte, J. Electrochem. Soc. 134(1987) 2379-2382. doi:10.1149/1.2100207.

[10]   T. Dai, L. Yang, X. Ning, D. Zhang, R.L. Narayan, J. Li,Z. Shan, A low-cost intermediate temperature Fe/Graphite battery for grid-scale energy storage, Energy Storage Mater. 25(2020) 801-810. doi:10.1016/j.ensm.2019.09.008.

[11] C. Peng, C.Z. Guan, J. Lin, S.Y. Zhang, H.L. Bao, Y. Wang, G.P. Xiao, G.Z. Chen,J.Q. Wang, A Rechargeable High-Temperature Molten Salt Iron-Oxygen Battery, Chemsuschem 11(2018) 1880-1886. doi:10.1002/cssc.201800237.

[12] B. Cui,S. Licht, A low temperature iron molten air battery, J. Mater. Chem. A 2(2014) 10577-10580. doi:10.1039/c4ta01290a.

[13] Y. Jin, K. Liu, J. Lang, D. Zhuo, Z. Huang, C.A. Wang, H. Wu,Y. Cui, An intermediate temperature garnet-type solid electrolyte-based molten lithium battery for grid energy storage, Nat. Energy 3(2018) 732-738. doi:10.1038/s41560-018-0198-9.

[14] B. Cui, J. Zhang, S. Liu, H. Xin, X. Liu, M. Lefler,S. Licht, Enhanced Iron Molten Air Battery Cycle Life and the Chemistry of the Nickel Oxide/Air Interface, J. Electrochem. Soc. 165(2018) A235-A243. doi:10.1149/2.0821802jes.

[15] D.J. Bradwell, H. Kim, A.H. Sirk,D.R. Sadoway, Magnesium–Antimony Liquid Metal Battery for Stationary Energy Storage, J. Am. Chem. Soc. 134(2012) 1895-1897. doi:10.1021/ja209759s.

[16] S.Y. Zhang, C. Peng, C.Z. Guan, G.P. Xiao,J.Q. Wang, Fabrication of Lanthanum Strontium Manganite Ceramics via Agar Gel Casting and Solid State Sintering, Materials 12(2019) 1-9. doi:10.3390/ma12060848.

[17] B. Cui, W. Xiang, S. Liu, H. Xin, X. Liu,S. Licht, A long cycle life, high coulombic efficiency iron molten air battery, Sustain. Energy & Fuels 1(2017) 474-481. doi:10.1039/c4ta01290a.

[18] Z. Zhu, D. Yu, Y. Yang, C. Su,J. Li, Gradient Li-rich oxide cathode particles immunized against oxygen release by a molten salt treatment, Nat. Energy 4(2019) 1049-1058. doi:10.1038/s41560-019-0508-x.

[19] W. Xiao,D.H. Wang, The electrochemical reduction processes of solid compounds in high temperature molten salts, Chem. Soc. Rev. 43(2014) 3215-3228. doi:10.1039/c3cs60327j.

[20] M.D. Susman, H.N. Pham, X. Zhao, D.H. West,J.D. Rimer, Synthesis of NiO Crystals Exposing Stable High-Index Facets, Angew. Chem. Int. Edit. 59(2020) 1-6. doi: 10.1002/anie.202003390.

[21] A. Dash, R. Vassen, O. Guillon,J. Gonzalez-Julian, Molten salt shielded synthesis of oxidation prone materials in air, Nat. Mater. 18(2019) 465-470. doi:10.1038/s41563-019-0328-1.

[22] M. Xiao, L. Zhang, B. Luo, M. Lyu, Z. Wang, H. Huang, S. Wang, A. Du,L. Wang, Molten-Salt-Mediated Synthesis of an Atomic Nickel Co-catalyst on TiO_2 for Improved Photocatalytic H_2 Evolution, Angew. Chem. Int. Edit. 59(2020) 7230-7234. doi:10.1002/anie.202001148.

[23] M.H. Habibi, L. Wang,S.M. Guo, Evolution of hot corrosion resistance of YSZ, $Gd_2Zr_2O_7$, and $Gd_2Zr_2O_7$ + YSZ composite thermal barrier coatings in Na_2SO_4 + V_2O_5 at 1050 °C, J. Eur. Ceram. Soc. 32(2012) 1635-1642. doi:10.1016/j.jeurceramsoc.2012.01.006.

[24] S. Kwon, S.-H. Cho, H.H. Nersisyan, J. Lee, J. Kang,J.-H. Lee, High-temperature stability of YSZ and MSZ ceramic materials in CaF_2-MgF_2-MgO molten salt system, J. Am. Ceram. Soc. 101(2018) 2074-2083. doi:10.1111/jace.15377.

[25] M. Yamauchi, K. Sugiura, T. Yodo,K. Tanimoto, Visualization of Electrolyte Volatile Phenomenon in MCFC : Effect of Electrolyte Filled, Trans. Visual. Soc. Japan 26(2006) 739-744.

[26] Z. Liu, H. Li, M. Zhu, Y. Huang, Z. Tang, Z. Pei, Z. Wang, Z. Shi, J. Liu, Y. Huang,C. Zhi, Towards wearable electronic devices: A quasi-solid-state aqueous lithium-ion battery with outstanding stability, flexibility, safety and breathability, Nano Energy 44(2018) 164-173. doi:10.1016/j.nanoen.2017.12.006.

[27]   D. Zhou, Y. Chen, B. Li, H. Fan, F. Cheng, D. Shanmukaraj, T. Rojo, M. Armand,G. Wang, A Stable Quasi-Solid-State Sodium–Sulfur Battery, Angew. Chem. Int. Edit. 57(2018) 10168 -10172. doi:10.1002/anie.201805008.

[28]   X. Xu, K. Lin, D. Zhou, Q. Liu, X. Qin, S. Wang, S.H. He, F. Kang, B. Li,G. Wang, Quasi-Solid-State Dual-Ion Sodium Metal Batteries for Low-Cost Energy Storage, Chem 6(2020) 1-17. doi:10.1016/j.chempr.2020.01.008.

[29]   Q. Pang, A. Shyamsunder, B. Narayanan, C.Y. Kwok, L.A. Curtiss,L.F. Nazar, Tuning the electrolyte network structure to invoke quasi-solid state sulfur conversion and suppress lithium dendrite formation in Li-S batteries, Nat. Energy 3(2018) 783-791. doi:10.1038/s41560-018-0214-0.

[30]   S.-J. Cho, G.Y. Jung, S.H. Kim, M. Jang, D.-K. Yang, S.K. Kwak,S.-Y. Lee, Monolithic heterojunction quasi-solid-state battery electrolytes based on thermodynamically immiscible dual phases, Energy Environ. Sci. 12(2019) 559-565. doi:10.1039/c8ee01503a.

[31]   X. Hu, Z. Li, Y. Zhao, J. Sun, Q. Zhao, J. Wang, Z. Tao,J. Chen, Quasi–solid state rechargeable Na-CO_2 batteries with reduced graphene oxide Na anodes, Sci. Adv. 3(2017) e1602396. doi:10.1126/sciadv.1602396.

[32]   V. Aravindan, C. Lakshmi,P. Vickraman, Investigations on Na^+ ion conducting polyvinylidenefluoride-co-hexafluoro-propylene/poly ethylmethacrylate blend polymer electrolytes, Curr. Appl. Phys. 9(2009) 1106-1111. doi:10.1016/j.cap.2008.12.009.

[33]   D.H. Le, P. Laffez, P. Daniel, A. Jouanneaux, N.T. Khoi,D. Siméone, Structure and phase component of ZrO_2 thin films studied by Raman spectroscopy and X-ray diffraction, Mat. Sci. Eng. B 104(2003) 163-168. doi:10.1016/S0921-5107(03)00190-9.

[34]   D. Gazzoli, G. Mattei,M. Valigi, Raman and X-ray Investigations of the Incorporation of Ca^{2+} and Cd^{2+} in the ZrO_2 Structure, J. Raman Spectrosc. 38(2007) 824-831. doi:10.1002/jrs.1708.

[35]   Y. Xia, Progress In Mossbauer Spectroscopy, Nucl. Sci. Tech. 1(1990) 24-31.

[36]   Z. Klencsár, E. Kuzmann,A. Vértes, User-friendly software for Mössbauer spectrum analysis, J. Radioanal. Nucl. Chem. 210(1996) 105-118. doi: 10.1007/BF02055410.

[37]   B. Ravel,M. Newville, Athena, Artemis, Hephaestus: data analysis for X-ray absorption spectroscopy using IFEFFIT, J. Synchrotron Radiat. 12(2005) 537-541. doi:10.1107/S0909049505012719.

[38]   J.J. Rehr, J.J. Kas, F.D. Vila, M.P. Prange,K. Jorissen, Parameter-free calculations of X-ray spectra with FEFF9, Phys. Chem. Chem. Phys. 12(2010) 5503-5513. doi:10.1039/b926434e.

Figures and captions
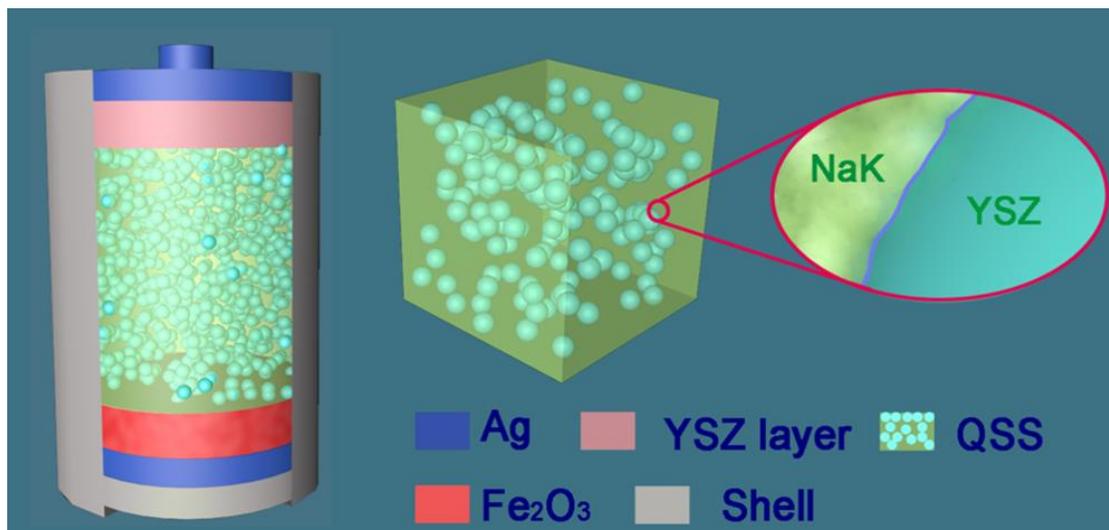
Figure 1. Schematic illustration of QSS-MIB.
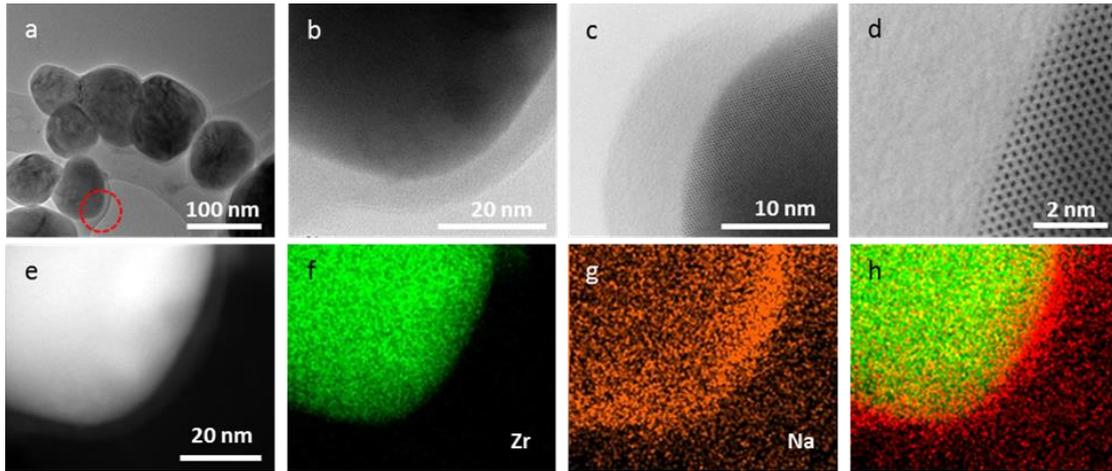
Figure 2. The morphology of QSS electrolyte. (a) a TEM image of the QSS electrolyte, (b, c, d) HR-TEM images showing the interfacial region between the NaK shell and YSZ nanoparticle at different magnifications, (e, f, g, h) EDS mappings of the QSS electrolyte.
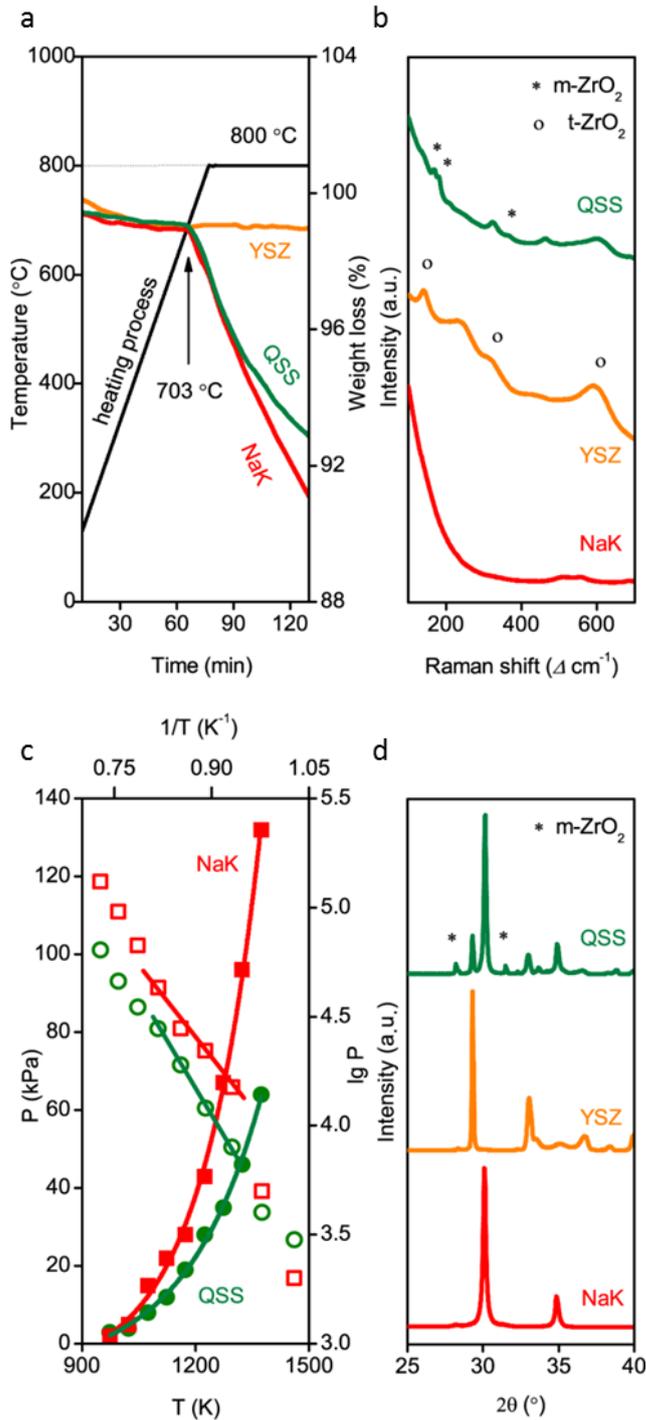
Figure 3. the physical properties of QSS electrolyte. (a) the TG curves of QSS electrolyte, NaK eutectic, and YSZ nanopowders. (b) Raman spectra of QSS electrolyte, NaK eutectic, and YSZ nanopowders at 800 □. (c) the measured evaporation pressure of QSS electrolyte and NaK eutectic at different temperatures. (d) XRD spectra of QSS electrolyte, NaK eutectic, and YSZ nanopowders, respectively.
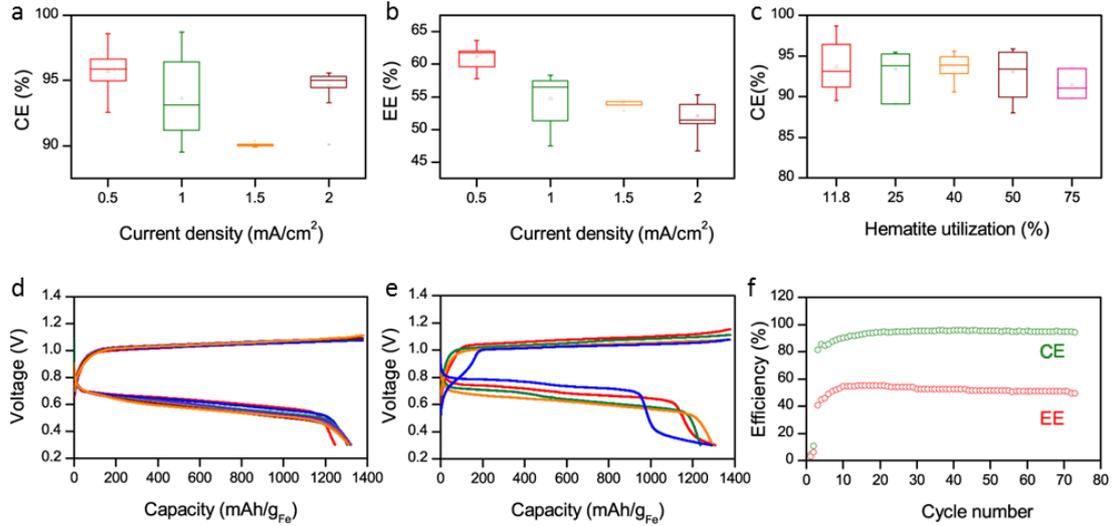
Figure 4. The performances of QSS-MIB. (a) the Columbic efficiencies of QSS-MIB at different discharge current densities, (b) the energy efficiencies of QSS-MIB at different discharge current densities, (c) the Columbic efficiencies of QSS-MIB at different hematite utilizations, (d) the charge-discharge curves of QSS-MIB in the cycle of 10th (red), 20th (blue), 30th (green), 40th (violet), 50th (gray), 60th (brown), 70th (orange), respectively, (e) the charge-discharge curves of QSS-MIB with the discharge current density of 0.5 (blue), 1 (red), 1.5 (green) and 2 (orange) mA cm^{-2}, respectively, (f) long-term cycling performance at 800 ▢ for 70 cycles.

14
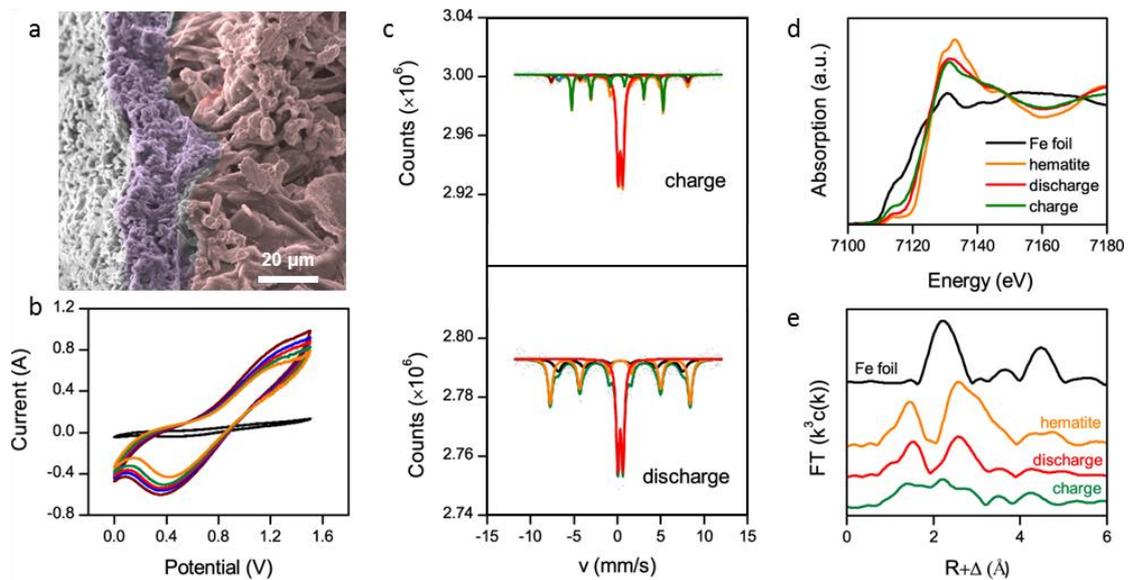
Figure 5. Investigation on the Fe$_2$O$_3$ negative electrode in QSS-MIB. (a) An SEM image of the solidified QSS electrolyte, (b) CVs of the silver negative electrode without (dark) and with the Fe$_2$O$_3$ loading in the QSS electrolyte at 800 □, with the scan rate of 10 mV s^{-1} (orange), 20 mV s^{-1} (green), 30 mV s^{-1} (red), 40 mV s^{-1} (blue), 50 mV s^{-1} (brown), respectively, (c) Mössbauer spectra, (d) XAFS, (e) FT-XAFS of the solidified QSS electrolyte of the charged and discharged natures, respectively.

Quasi-solid-state electrolyte for rechargeable high-temperature molten salt iron-air battery

Experimental section

Battery fabrication. The silver wires (99.99%, Jinchang Alloy Co. Ltd., Shanghai, China) with the diameter of 1 mm was coiled and immerged into the room-temperature saturated iron trichloride aqueous solution for absorbing iron ions, and then treated at 200 □ for dehydration and 800 □ for calcination, respectively. The preparation of negative electrode was completed after several times of absorption, dehydration and calcination, until the deposition weight reached ~0.15g. The iron trichloride was purchased from Aladdin reagent (Shanghai) Co., Ltd., China. The YSZ plate (8 mol%) with the thickness of 0.8 mm was prepared by direct tablet compressing 8 mol% YSZ powders (Tianrao Industrial Co. Ltd., Qingdao, China) after annealing treatment at 800 □ for 3 h and at 1400 □ for 2 h, respectively. The silver positive electrode was fabricated by coating conductive silver paste (Shanghai research institute of synthetic resins, Shanghai, China) on one side of YSZ plate, and silver wires with the diameter of 1 mm were stuck on silver positive electrode after drying at 200 □. To construct a typical bi-phase molten salt iron air battery, the as-prepared negative electrode was first placed in the bottom of an alumina crucible which were then filled with the Na_2CO_3 (15 g), K_2CO_3 (15 g) and YSZ nanopowders (30 g) mixture. The sodium carbonate was purchased from Tianjin Zhiyuan Co., Ltd., China, the potassium carbonate were purchased from Tianjin Bodi Co., Ltd., China. The whole crucible was placed in an oven (made by Hefei Kejing materials technology Co., Ltd., China) which provides a constant high temperature at 800 □, and the as-prepared positive electrode was placed on the quasi-solid-state electrolyte with a close contact.

Electrochemical experiments. The battery with the area of ~5 cm^2 of negative silver electrode was investigated in the mode of recycling constant current charge at 20 mA within 30 min and constant current discharge at 0.5, 1, 1.5 and 2 mA/cm^2, respectively, with a cutoff voltage of 0.5 V. The columbic efficiency was evaluated by the ratio of charge/discharge electric quantities, which were calculated by integrating the charge/discharge current per second. The energy efficiency was evaluated by the ratio of charge/discharge energies, which were calculated by integrating the product of charge/discharge current and voltage per second. The output specific energy was calculated by the product of hematite utilization, energy efficiency and the theoretical energy capacity of iron-Air battery (Gibbs free energy change for $2Fe +1.5O_2 = Fe_2O_3$, 1.35 kWh kg^{-1} at 800 ℃). All the electrochemical experiments were performed on LANHE CT2001A battery test system. Cyclic voltammetry curves in the range from 0 to 2 V with the scanning rate of 20 mV s^{-1}, and electrochemical impedance spectra in the range from 0.1 Hz to 10000 Hz were collected by Princeton 4000+ electrochemical workstation. All the experiments were executed in air at 800 □.

Materials characterization. Aberration-corrected high-angle annular dark field-STEM and STEM-EDX images were obtained on a JEM-ARM200F transmission electron microscopy, which incorporated with double spherical aberration correctors. The SEM and EDX images were obtained on a Merlin Compact scanning electron microscopy. The Raman spectroscopy

measurements were conducted at 800□ using an HORRIBA Confocal Raman microscope with the 532 nm laser excitation. The neutron powder diffraction experiments were carried out at 800 □ using the high resolution neutron powder diffractometer (HRND) at China Mianyang Research Reactor (CMRR) with the wavelength of λ=1.8846 Å, all the samples were sealed in stainless steel tubes. XRD patterns were obtained on a Bruker D8 Advanced diffractometer using CuKa radiation (l=1.5418 a) with a scanning rate of 2° min^{-1} when the voltage and current was 40 kV and 40 mA, respectively. The TG curves were obtained on a NETZSCH STA 449F3, with a constant rising temperature mode of 10 □ min^{-1} and a constant temperature mode. The evaporation experiments were carried out in a vacuum tubular furnace (made by Hefei Kejing materials technology Co., Ltd., China). The samples were vacuumized in the vacuum tubular furnace and the pressure was recorded at different temperatures when the value was stable. Mossbauer spectra were measured using a constant acceleration transmission mode with a 57Co/Rh source at room temperature. The velocity was calibrated with a 25 mm a-Fe foil, and the isomer shift was relative to the center of a-Fe at room temperature. All the Mössbauer data have computer-fitted via MossWinn, assuming several hyperfine components made of absorption peaks with Lorentzian line shapes. Fe K-edge X-ray absorption spectroscopy data were collected at beamline XAFCA of the Singapore Synchrotron Light Source. Data were recorded in transmission mode. Acquired XAFS data were processed with the ATHENA program and analysed in the ARTEMIS program integrated with Demeter software package, and the theoretical phase and amplitude functions were calculated using FEFF 9.0. All the EXAFS oscillations were extracted from the normalized XAS spectra by subtracting the atomic background using a cubic spline fit to k3-weighted data, where k is the photoelectron wave number. The χ(k) functions were then Fourier transformed into R-space.

Theoretical viscosity calculation. The theoretical viscosity of molten NaK via Arrhenius viscosity formula[1]:

$$\ln \eta = \sum_{i=1}^{n} x_i \ln \eta_i \qquad \text{(equ 1)}$$

Where η is the viscosity of molten eutectic, x_i and η_i is the mole fraction and viscosity of i. The relation between viscosity and temperature of Na_2CO_3 and K_2CO_3 are shown in equ 2 and equ 3[2]:

$$\eta = 3.832 * 10^{-5} * e^{\frac{26260}{RT}} \qquad \text{(equ 2)}$$

$$\eta = 1.161 * 10^{-5} * e^{\frac{29487}{RT}} \qquad \text{(equ 3)}$$

Where R is molar gas constant, 8.314 J/(mol·K), T is temperature, K.

When the mass ratio of Na_2CO_3 and K_2CO_3 is 1:1, the mole fraction of Na_2CO_3 is 0.57 and 0.43 for K_2CO_3. We can obtain the relationship between viscosity and temperature of NaK molten salt is shown in equ 4:

$$\eta = 2.293 * 10^{-5} * e^{\frac{27647}{RT}} \qquad \text{(equ 4)}$$

[1] REPORT ON THE HELIUM SYSTEM EXPERIMENT AT OAK RIDGE, TENNESSEE Authors:Newson, H WPublication Date:1956-10-31Research Org.:Brookhaven National Lab., Upton, N.Y.OSTI Identifier:4369134 Report Number(s):M-4461NSA.

[2] G. J. Janz, R. P. T. Tomkins, Physical properties data compilations relevant to energy storage. IV. Molton salts: data on additional single and multi-component salt systems, NASA STI/Recon Technical Report N. 80., Washington, 1981, pp. 131-124.
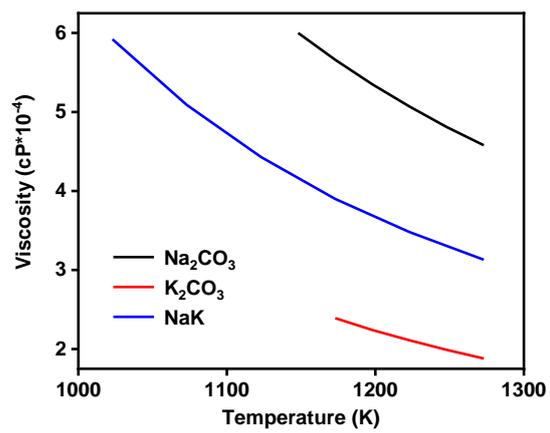
Figure S1. The viscosity of molten NaK at different temperatures.
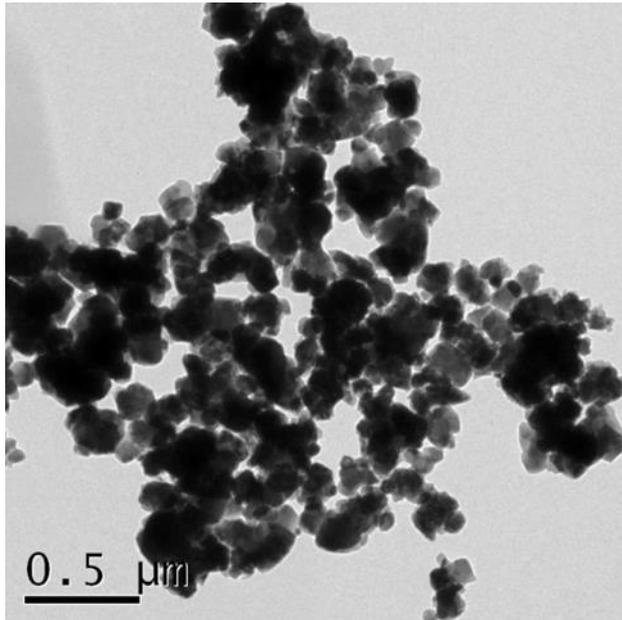
Figure S2. The TEM image of YSZ nanopowders.
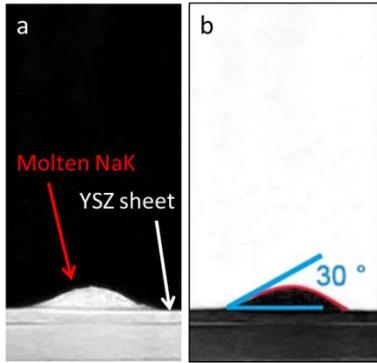
Figure S3. The photograph of molten NaK on YSZ layer (a) and the wetting angle between YSZ layer and molten NaK (b).
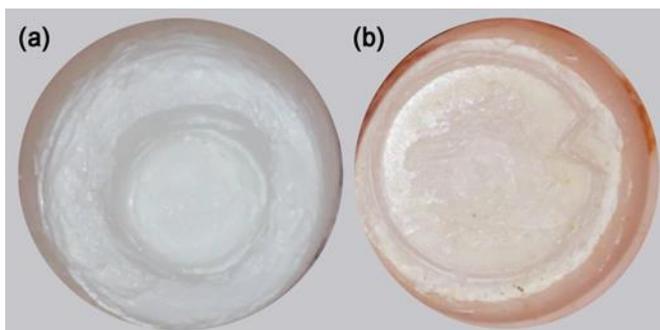
Figure S4. The digital pictures of QSS electrolyte after extruded in different shapes at 850 □.

Figure S5. The top view of pure NaK molten salt and NaK-YSZ mixtures with different mass ratio at 800 °C, top view and right view at room temperature, molten NaK (a, b, c), YSZ:NaK 1:5 (d, e, f), YSZ:NaK 2:3 (g, h, i), YSZ:NaK 1:1 (j, k, l), and YSZ:NaK 3:2 (m, n, o).
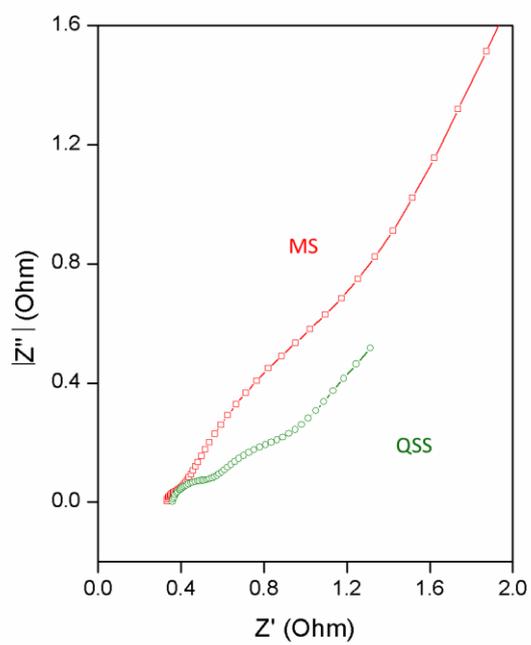
Figure S6. (a) EIS analysis of molten salt (MS) and QSS electrolyte, respectively.
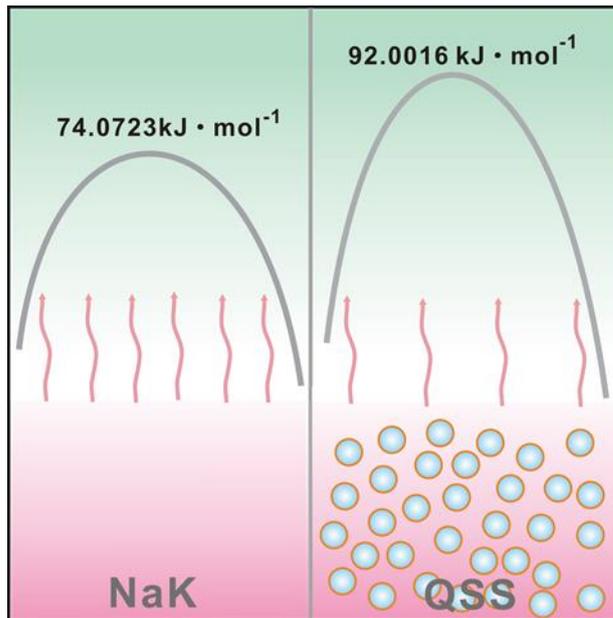
Figure S7. The illustration of the energy of evaporation for the QSS electrolyte and NaK eutectic, respectively.
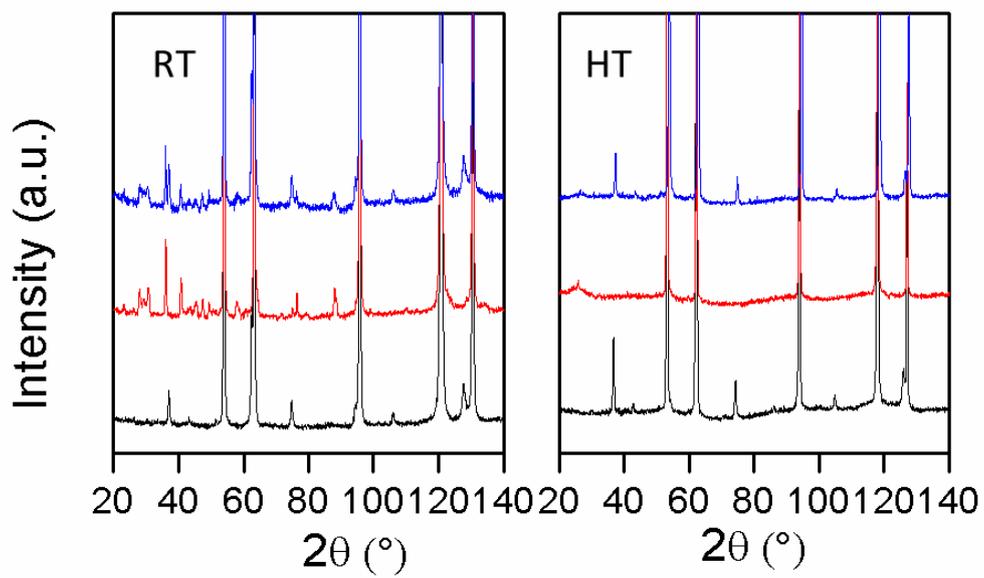
Figure S8. HRND spectra of QSS (blue), NaK (red) eutectic and YSZ nanopowders (dark) at room temperature and 800 □, respectively.
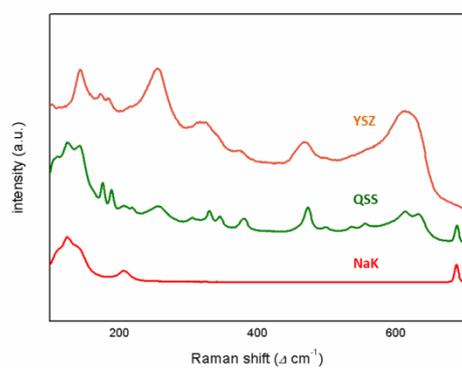
Figure S9. Room-temperature Raman spectra of QSS electrolyte, YSZ powders and NaK eutectic, respectively.
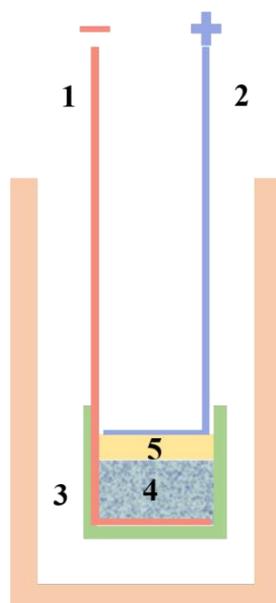
Figure S10. Schematic illustration of the testing system for QSS-MIB, showing (1) the Fe_2O_3-coated Ag wire negative electrode, (2) positive electrode (Ag wire), (3) alumina crucible, (4) QSS electrolyte, (5) YSZ sheet.
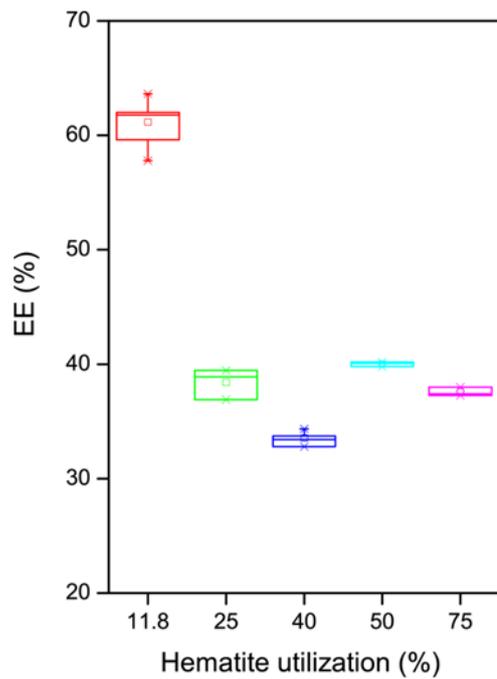
Figure S11. The energy efficiency of QSS-MIB with different hematite utilizations.
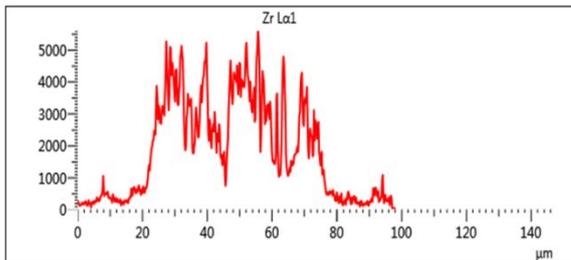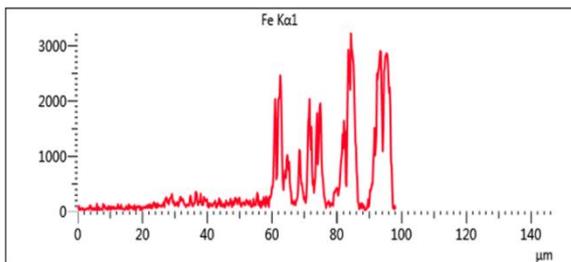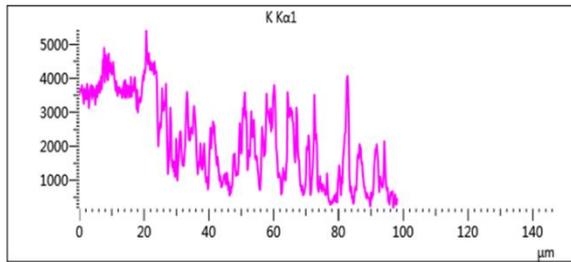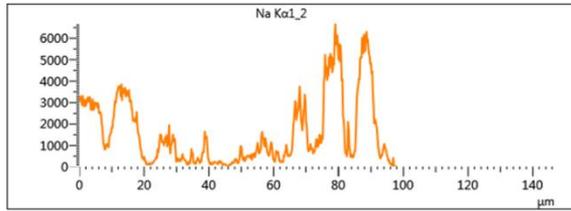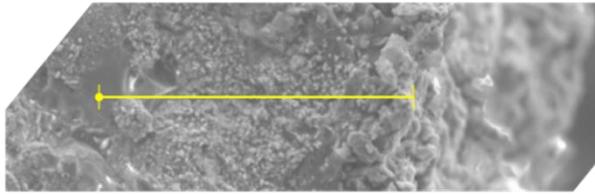
Figure S12. The distribution of Fe, Zr, Na and K near the interface between the QSS electrolyte and the distinctive layer.
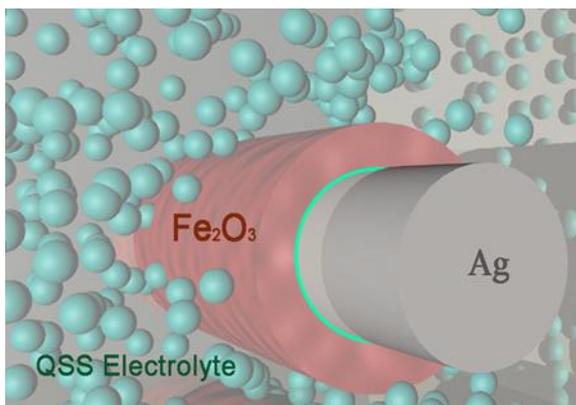
Figure S13. The illustration of 3PI on the negative electrode in QSS-MIB.
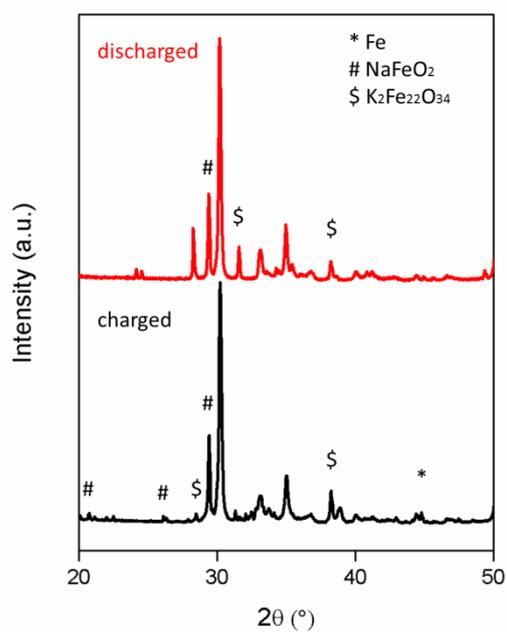
Figure S14. Room-temperature XRD spectra of solidified QSS electrolyte of the charged and discharged natures, respectively.

Table S1 the comparison of battery performance parameters.	Bi-phase electrolyte structured MIB[1]	QSS-MIB in this work
energy efficiency	~37%, highest	~61%, highest
Fe^0 utility	~0.35%	75%
cycle life	~3.5h	~113h

1. C. Peng, C. Z. Guan, J. Lin, S. Y. Zhang, H. L. Bao, Y. Wang, G. P. Xiao, G. Z. Chen and J. Q. Wang, *Chemsuschem*, 2018, 11, 1880-1886.

Table S2. Mössbauer data of the solidified QSS electrolyte after charge and discharge, respectively.

	Magnetic(1) Spinel-A site $K_2Fe_{22}O_{34}$					Magnetic(1) Spinel-B site $K_2Fe_{22}O_{34}$					Magnetic(3) Fe(0)					Fe(III) Doublet (1) $NaFeO_2$				
	IS	QS	LW	MF	Area	IS	QS	LW	MF	Area	IS	QS	LW	MF	Area	IS	QS	LW	MF	Area
	(mm/s)			(T)	(%)	(mm/s)			(T)	(%)	(mm/s)			(T)	(%)	(mm/s)			(T)	(%)
Charge	0.64		0.62	45.91	9.24	0.27		0.36	49.01	7.25	0.00		0.27	32.78	26.40	0.35	0.53	0.42		57.11
Discharge	0.35		1.06	44.74	21.48	0.32		0.57	50.15	42.05						0.34	0.60	0.44		36.47